The viral F-box protein P0 induces an ER-derived autophagy degradation pathway for the clearance of membrane-bound AGO1

Simon Michaeli[a], Marion Clavel[a], Esther Lechner[a], Corrado Viotti[a], Jian Wu[b], Marieke Dubois[a,c], Thibaut Hacquard[a], Benoît Derrien[a,d], Esther Izquierdo[e], Maxime Lecorbeiller[a], Nathalie Bouteiller[f], Julia De Cilia[a], Véronique Ziegler-Graff[a], Hervé Vaucheret[f], Gad Galili[b], and Pascal Genschik[a,1]

[a]Institut de Biologie Moléculaire des Plantes, Centre National de la Recherche Scientifique, Unité Propre de Recherche 2357, Conventionné avec l'Université de Strasbourg, 67084 Strasbourg, France; [b]Department of Plant and Environmental Sciences, Weizmann Institute of Science, 76100 Rehovot, Israel; [c]VIB-UGent Center for Plant Systems Biology, Ghent University, 9052 Ghent, Belgium; [d]DNA SCRIPT, 75014 Paris, France; [e]Biochimie et Physiologie Moléculaire des Plantes, Université Montpellier, CNRS, Institut National de la Recherche Agronomique, SupAgro, 34060 Montpellier, France; and [f]Institut Jean-Pierre Bourgin, UMR1318, Institut National de la Recherche Agronomique, AgroParisTech, CNRS, Université Paris-Saclay, 78000 Versailles, France

Edited by Mark Estelle, University of California San Diego, La Jolla, CA, and approved September 23, 2019 (received for review July 17, 2019)

RNA silencing is a major antiviral defense mechanism in plants and invertebrates. Plant ARGONAUTE1 (AGO1) is pivotal in RNA silencing, and hence is a major target for counteracting viral suppressors of RNA-silencing proteins (VSRs). P0 from *Turnip yellows virus* (TuYV) is a VSR that was previously shown to trigger AGO1 degradation via an autophagy-like process. However, the identity of host proteins involved and the cellular site at which AGO1 and P0 interact were unknown. Here we report that P0 and AGO1 associate on the endoplasmic reticulum (ER), resulting in their loading into ER-associated vesicles that are mobilized to the vacuole in an ATG5- and ATG7-dependent manner. We further identified ATG8-Interacting proteins 1 and 2 (ATI1 and ATI2) as proteins that associate with P0 and interact with AGO1 on the ER up to the vacuole. Notably, ATI1 and ATI2 belong to an endogenous degradation pathway of ER-associated AGO1 that is significantly induced following *P0* expression. Accordingly, ATI1 and ATI2 deficiency causes a significant increase in posttranscriptional gene silencing (PTGS) activity. Collectively, we identify ATI1 and ATI2 as components of an ER-associated AGO1 turnover and proper PTGS maintenance and further show how the VSR P0 manipulates this pathway.

RNA silencing | autophagy | *Arabidopsis*

In eukaryotes, gene silencing is essential for development and plays important roles in response to biotic and abiotic stresses, as well as in epigenetic control of transposable elements. RNA silencing involves the processing of double-stranded (ds)RNA by Dicer-like RNase III enzymes, into small RNAs (sRNAs) of 21 to 24 nucleotides in length (1). All types of sRNAs are then incorporated into a protein complex called RISC (RNA-induced silencing complex) that invariably contains a member of the highly conserved Argonaute (AGO) protein family (2, 3). These RISCs are programmed by the bound sRNAs to specifically interact with transcripts based on sequence complementarity, resulting in messenger RNA (mRNA) cleavage, translational repression, or chromatin modification. An important class of endogenous sRNAs is microRNAs (miRNAs) (4, 5), which repress the expression of one or more target mRNAs and have been predicted to control a significant proportion of the transcriptome (6). Important functions for sRNAs have also emerged in the study of host–pathogen interactions. In particular, RNA silencing plays a key role in antiviral defense in plants and invertebrates, where populations of sRNAs are produced in infected cells directly by processing dsRNA molecules derived from the viral genome (7, 8). These virus-derived small interfering RNAs (siRNAs) are then incorporated into an antiviral RISC and turned back onto viral RNAs to trigger their degradation.

In the model plant *Arabidopsis thaliana* (hereafter referred to as *Arabidopsis*), the AGO protein family is composed of 10 members divided into 3 major clades based on their protein similarity (9). Among them, AGO1 plays a central role in both miRNA- and siRNA-directed silencing (10). Hence, AGO1 loaded with sRNAs mediates endonucleolytic cleavage of target transcripts (11), but a fraction of transcripts also evades slicing and instead undergoes translation repression (12, 13). Moreover, AGO1 plays an important function in the biogenesis and control of secondary siRNAs (14–16). Finally, besides its regulatory role of endogenous gene expression through miRNAs and endogenous siRNAs, AGO1 is paramount in antiviral defense, and, consequently, various *ago1* mutants exhibit enhanced susceptibility to virus infection (17, 18). However, as a counter defense strategy, viruses have acquired various viral suppressors of RNA silencing (VSRs), which can target different steps of the RNA silencing pathway (19, 20).

Previous work from our laboratory and others revealed that the VSR protein P0 from Polerovirus encodes an F-box protein that hijacks the host S-phase kinase-associated protein1 (SKP1)-cullin 1 (CUL1)-F-box protein (SCF) ubiquitin-protein ligase (E3) to promote AGO1 degradation (21–24). Although different

Significance

The viral suppressor of RNA silencing P0 is known to target plant antiviral ARGONAUTE (AGO) proteins for degradation via an autophagy-related process. Here we utilized P0 to gain insight into the cellular degradation dynamics of AGO1, the major plant effector of RNA silencing. We revealed that P0 targets endoplasmic reticulum (ER)-associated AGO1 by inducing the formation of ER-related bodies that are delivered to the vacuole with both P0 and AGO1 as cargos. This process involves ATG8-interacting proteins 1 and 2 (ATI1 and ATI2) that interact with AGO1 and negatively regulate its transgene-silencing activity. Together, our results reveal a layer of ER-bound AGO1 post-translational regulation that is manipulated by P0 to subvert plant antiviral defense.

Author contributions: S.M., M.C., C.V., and P.G. designed research; S.M., M.C., E.L., C.V., J.W., M.D., T.H., B.D., E.I., M.L., N.B., and H.V. performed research; J.W., J.D.C., V.Z.-G., and G.G. contributed new reagents/analytic tools; S.M., M.C., E.L., C.V., M.D., T.H., B.D., E.I., M.L., V.Z.-G., H.V., and P.G. analyzed data; and P.G. wrote the paper with the participation of S.M.

The authors declare no competing interest.

This article is a PNAS Direct Submission.

[1]To whom correspondence may be addressed. Email: pascal.genschik@ibmp-cnrs.unistra.fr.

This article contains supporting information online at www.pnas.org/lookup/suppl/doi:10.1073/pnas.1912222116/-/DCSupplemental.

First published October 18, 2019.

Poleroviruses encode P0 proteins that lack sequence similarity, most of them can mediate the decay of AGOs (25, 26). SCF-type ubiquitin E3 ligases promote ubiquitylation of their substrates, which serves as a signal for proteasomal degradation (27, 28). However, inhibition of the proteasome was unable to block P0-mediated degradation of AGO1 (22). Instead, it was shown that AGO1 degradation was blocked by pharmacological inhibition of trafficking pathways that lead to the vacuole, including macroautophagy, and that *P0* expression leads to an accumulation of AGO1 in vacuolar inclusions (29).

Macroautophagy (hereafter referred to as autophagy) is an evolutionary conserved intracellular degradation and recycling mechanism involving the generation of a specialized double membrane termed the phagophore, which likely emanates from the endoplasmic reticulum (ER) (30, 31). The phagophore captures cytosolic content (cargo) and then seals to form an autophagosome that delivers the cargo to cellular lytic compartments (lysosomes in animals or vacuoles in yeast and plants). The autophagy process requires more than 40 proteins to function, most of which are annotated as autophagy-related proteins (ATG) (32–34). Under energetically demanding stress, cells induce nonselective autophagy, by which cytosolic content is degraded. However, under specific stress and developmental conditions, subcellular structures are cleared by selective autophagy (34–36), a process implying specialized cargo receptors that anchor the cargo to autophagy machinery components. In many cases, cargo receptors interact with ATG8 proteins, which are known to decorate both the inner and outer membranes of the autophagosome and are involved in autophagosome maturation as well as in their fusion with the lytic compartment. Frequently, ubiquitylation serves as a signal for the recognition of cargoes destined for selective autophagy (36). In plants, only a few selective autophagy receptors have been identified (34). Among them are neighbor of BRCA 1 (NBR1), a functional hybrid of mammalian p62 and NBR1 autophagy receptors, which targets ubiquitylated protein aggregates in plant stress responses (37, 38) and virus particles (39), tryptophan-rich sensory protein (TSPO) that can target plasma-membrane based aquaporins (40), and RPN10, which degrades inactive 26S proteasomes (41). ATG8-interacting 1 and 2 (ATI1 and ATI2), on the other hand, are transmembrane proteins reported to localize to ER- and plastid-derived vesicles that traffic to the vacuole (42, 43). Although ATI1/2 interact with ATG8f and rely on core autophagy machinery to reach the vacuole, ATI1/2 decorated bodies are generally distinct from ATG8-decorated autophagosomes, and their function on the ER is still poorly understood (42).

The pivotal role of autophagy during viral infection in plants has only recently emerged, with reports demonstrating both antiviral and proviral functions (44, 45). At present, little is known about the mechanism of P0-mediated AGO1 protein degradation. The viral F-box protein P0 has been proposed to act upstream of AGO1 loading (24), as it is very effective in degrading newly synthesized AGO1 after transient expression in tobacco leaves, but not endogenous preassembled AGO1 complex. We recently found that P0 recognizes the DUF1785 domain of AGO1 to enable its degradation (46), but where this occurs at the subcellular level is unknown. Notably, AGO1 protein also decays via a similar pathway in a P0-independent manner, when miRNA production or stability is compromised (29). However, the assumption that the AGO1 protein decays via autophagy in a P0-dependent and independent context mainly relies on the use of pharmacological treatments known to inhibit autophagy, and whether this mechanism involves a cargo receptor is presently unknown.

Here we took advantage of the VSR P0 of *Turnip yellows virus* (TuYV) to induce and monitor *Arabidopsis* AGO1 degradation dynamics. We report that the ER membrane is the main site where AGO1 and P0 encounter each other, forming ER-associated bodies that contain both proteins and are delivered to the vacuole. These bodies require functional autophagy to reach the vacuole, yet autophagy deficiency is unable to block P0-mediated AGO1 degradation. We further identified the ER-localized proteins ATI1/2 (42, 43) as proteins that mediate the delivery of both AGO1 and P0 as cargoes en route to the vacuole. ATI1 directly interacts with AGO1, and *P0* expression is sufficient to induce a flux of ATI1-decorated vesicles to the vacuole. Deficiency in both *ATI1/2* does not lead to a marked increase of AGO1 protein steady-state levels, yet attenuates membrane-associated AGO1 degradation following P0 induction and results in significantly increased sense transgene-mediated post-transcriptional gene silencing (S-PTGS) activity. Together, our results suggest that ER-bound AGO1 is targeted for vacuolar degradation and that the VSR P0 evolved to manipulate this pathway.

Results

P0 Encounters AGO1 on the ER and Both Proteins Are Codelivered to the Vacuole. Previous reports indicated that AGO1 appears in membrane-bound and membrane-free (soluble) forms (13, 47), and that miRNAs copurify with membrane-bound polysomes through their association with AGO1 (48). To learn more about P0-mediated AGO1 degradation, we first examined whether either of the 2 AGO1 pools is more prone to degradation than the other. To this end, we used the XVE:P0-myc line (29), in which P0-myc expression is under the control of a β-Estradiol (β-Es)–inducible promoter. We treated XVE:P0-myc seedlings with either dimethyl sulfoxide (DMSO) as mock (−) or β-Es (+) and evaluated AGO1 protein level in soluble and microsomal fractions (Fig. 1*A*). The marker for ER lumen (BiP) was enriched in the microsomal fraction, whereas the cytosolic enzyme UDP-glucose pyrophosphorylase (UGPase) was almost absent, yet enriched in the soluble fraction. Most AGO1 protein was detected in microsomes, and its abundance decreased after β-Es treatment. Although P0-myc was also present in the soluble fraction, the P0-myc detected in the microsomes is likely the cause of membrane-bound AGO1 decay (Fig. 1*A*). Additionally, the presence of P0-myc in the soluble fraction enables the degradation of the soluble pool of AGO1 and AGO4, the latter being enriched in the soluble fraction as previously reported (48). Since miRNA localization to membranes arises from their association with AGO1, membrane-associated AGO1 degradation by P0-myc should lead to a decrease in miRNA in the microsomal fraction. Indeed, while the levels of some inspected miRNAs (miR173, miR167, and miR159) were largely unaffected in the soluble fraction, their abundance was markedly decreased in the presence of P0-myc in microsomes, while 24-nt siR1003 that associates with AGO4 was only detected in the soluble fraction (*SI Appendix*, Fig. S1). From these results, we conclude that the viral F-box P0 exerts its activity on both soluble and membrane-bound AGO1, and that P0-mediated degradation of membrane-associated AGO1 results in decreased miRNA-programmed RISC in membranes (*SI Appendix*, Fig. S1).

To determine the identity of the intracellular membranes with which P0 may associate, its coding sequence was fused to either GFP (P0-GFP) or mRFP (P0-mRFP) under the control of the constitutive Cauliflower Mosaic Virus 35S promoter. Additionally, P0-mRFP was also expressed under the control of the β-Es–inducible promoter (XVE:P0-mRFP). Transient expression assays in *Nicotiana benthamiana* revealed that both P0-GFP and P0-mRFP are as efficient as the previously reported P0-myc in degrading AGO1 and that mutating the P0-mRFP F-box domain (XVE:P0^{LP}-mRFP) fully abolished AGO1 degradation (*SI Appendix*, Fig. S2*A*). Expression of P0-GFP along with the ER marker mCherry-HDEL in *N. benthamiana* leaf cells revealed that the viral F-box protein partially overlaps with the ER and labels ER-associated bodies (*SI Appendix*, Fig. S2*B* and Movie S1). Next, we generated XVE:P0-mRFP *Arabidopsis* stable lines

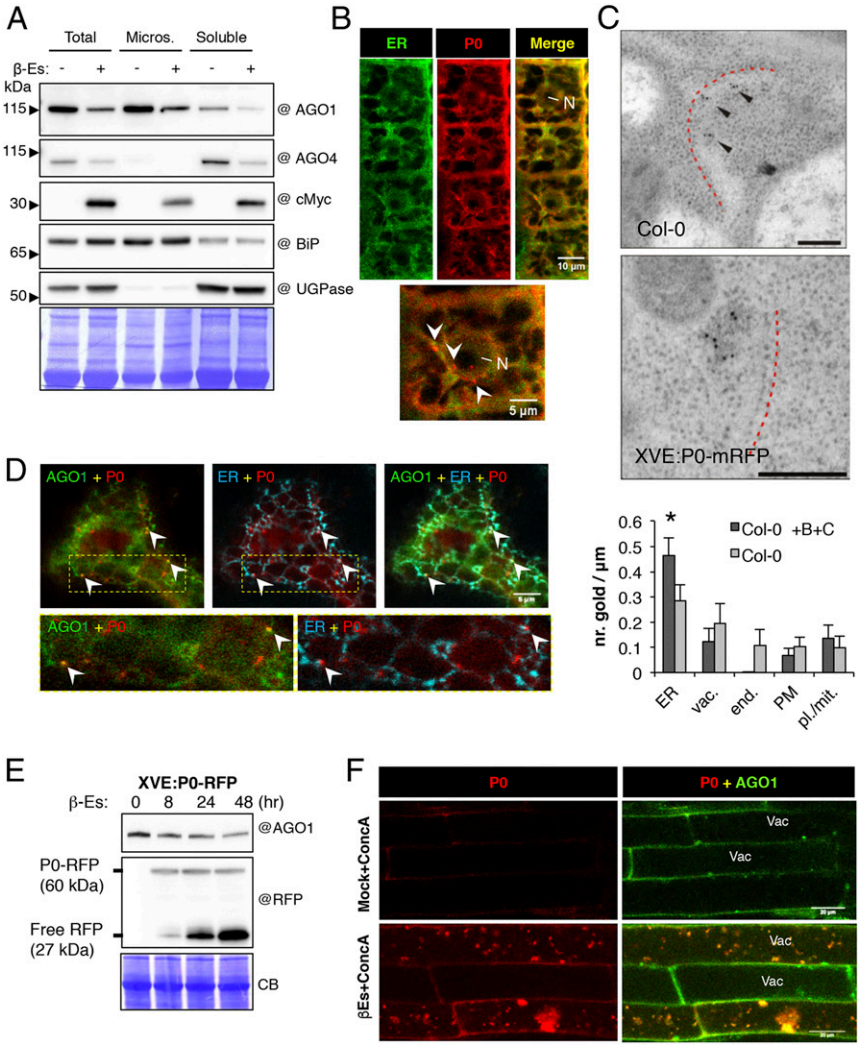

Fig. 1. P0 and AGO1 colocalize in ER-associated bodies that are destined to the vacuole. (*A*) Immunoblot analysis of total, pellet (Microsomal), and supernatant (Soluble) protein preparations from XVE:P0-myc 7-d-old seedlings grown on Murashige and Skoog (MS) plates with either DMSO (–) or 10 μM β-Es (+). Blots were probed with antibodies raised against *Arabidopsis* AGO1, AGO4, the c-MYC tag, Luminal binding proteins BiP1/BiP2/BiP3 (BiP), and UGPase. Coomassie blue (CB) staining serves as loading control. (*B*) CLSM imaging of *Arabidopsis* root meristematic cells expressing P0-mRFP (red signal) and stained with ER-Tracker blue-white DPX (ThermoFisher; green signal). Both the merged image of the signals and an enlarged image of one of the cells are presented. Positions of the nucleus (N) and P0-mRFP labeled bodies (arrowheads) are indicated. (*C*) (*Top* and *Middle*) TEM imaging of ER (denoted by a dashed red line) in a root cell that underwent immunogold labeling using @AGO1 antibodies. Arrowheads mark the sites of gold particles in *Top*. Both Col-0 and the XVE:P0-mRFP line were treated with β-Es and ConcA. (Scale bars: 200 nm.) (*Bottom*) A graph showing quantification of gold particles associated with the ER, tonoplast (vac.), endosomes (end.), plasma membrane (PM), and plastid + mitochondria (pl./mit.) outer membranes. Quantification was done in samples from β-Es and ConcA treated (+B+C), or untreated, Col-0 plants. Values represent mean ± SEM. Asterisk (*) denotes statistical significance of gold particle numbers along the ER compared to the other membranes within the +B+C treated plants, $P < 0.05$ (Mann–Whitney *U* test). (*D*) (*Top*) CLSM imaging of a tobacco leaf epidermal cell transiently expressing GFP-AGO1 (AGO1), CFP-HDEL (ER), and P0-mRFP (P0). (*Bottom*) Enlargements of the areas bordered by yellow rectangles in *Top*. Bodies exhibiting both P0 and AGO1 signals are highlighted with arrowheads. (*E*) Immunoblot analysis of total proteins from XVE:P0-mRFP seedlings treated with β-Es for 0, 8, 24, and 48 h to induce P0-mRFP expression. Blots were probed with specific antibodies as indicated, and CB staining serves as loading control. (*F*) CLSM imaging of the vacuolar focal plane of root elongation zone cells from an *Arabidopsis* line harboring pAGO1:GFP-AGO1 and XVE:P0-mRFP and treated with β-Es and ConcA or mock (DMSO) and ConcA. Vacuole lumen is indicated (Vac).

that exhibit efficient P0-mRFP induction following treatment with β-Es (*SI Appendix*, Fig. S2*C*). Staining root cells that express P0-mRFP with ER-Tracker (Thermo Fisher Scientific) demonstrated again its partial association with the ER (Fig. 1*B*). However, in this system, a broader distribution of the signal along the ER was observed with the addition of bodies that appear associated with the ER-Tracker signal. These observations suggest that the ER might be a site from which membrane-bound AGO1 is targeted for degradation.

Previously, it was reported that AGO1 localizes on the ER membrane (13, 48). We reexamined this by utilizing both fluorescence and electron microscopy (EM) techniques. First, we transiently expressed 35S:GFP-AGO1 in *N. benthamiana* epidermal leaf cells along with the ER marker mCherry-HDEL and focused on the cytosolic focal planes. This revealed partial association of AGO1 with the ER in 52% of the examined cells ($n = 32$) (*SI Appendix*, Fig. S3 *A*, *Top*), while, in other transformed cells, the signal was cytosolic (*SI Appendix*, Fig. S3 *A*, *Bottom*). To gain insight into the localization of the endogenous AGO1 and the impact of P0 expression on AGO1 localization at the ultrastructural level, we treated Col-0 and XVE:P0-mRFP seedlings with β-Es and concanamycin A (ConcA; an inhibitor of vacuolar degradation),

and analyzed root cells by immuno-EM (IEM) with the anti-AGO1 antibody. We reasoned that using Col-0 plants that were subjected to the same chemicals as XVE:P0-mRFP plants would allow the assessment of the effect of P0 per se, excluding the possible influence of the drugs. In Col-0 seedlings, the compartment showing the highest AGO1 labeling density on its limiting membrane was the ER (Fig. 1 *C*, *Top* and *Bottom*). In P0-mRFP seedlings, AGO1 labeling was detected in few cases on electron-dense structures adjacent to the ER membrane (Fig. 1 *C*, *Middle* and *SI Appendix*, Fig. S4). Such structures were not detected in the Col-0 samples. This suggests that *P0* expression may result in the aggregation of AGO1 in ER-associated structures. Quantification revealed that most of the gold particles were present along the ER compared to all other membranes in both treated and untreated Col-0. However, this enrichment was only statistically significant in the chemically treated seedlings (Mann–Whitney *U* test, $P < 0.05$) (Fig. 1 *C*, *Bottom*). This might be due to the inhibitory impact of ConcA on vacuolar degradation, resulting in more protein lingering on the ER membrane. Hence, although AGO1 may associate with several membranes and appear also in a soluble form, our results corroborate previous reports pointing toward the ER as a major site for membrane-bound AGO1 (13, 48). Notably, *P0* expression affects the morphology of ER-associated AGO1. In support of this, coexpression of GFP-AGO1 and P0-mRFP in *N. benthamiana* leaves revealed that both proteins exhibited an ER-like expression pattern and colocalized in bodies (*SI Appendix*, Fig. S3*B*). To see whether these structures are indeed associated with the ER, we expressed GFP-AGO1 and P0-mRFP along with an ER marker, CFP-HDEL (Fig. 1*D*). Structures containing P0-mRFP were indeed closely associated with the ER, and some were also enriched with the GFP-AGO1 signal (Fig. 1*D*, white arrowheads). Moreover, time-lapse imaging revealed the motile nature of the P0 and AGO1 labeled bodies (Movie S2). Note that the colocalization of GFP-AGO1 and P0-mRFP was only detected at early time points of their expression, that is, 24 h to 40 h following agroinfiltration (hfa). At later time points, that is, 48 hfa to 96 hfa, AGO1-labeled foci were no longer detected, probably due to AGO1 degradation. Moreover, in these transient expression assays, GFP-AGO1 and P0-mRFP were also occasionally detected in the nuclei (*SI Appendix*, Fig. S3*C*).

Next, we took advantage of the relative stability of mRFP to examine whether P0-mRFP is delivered to vacuoles. Total protein extraction from XVE:P0-mRFP seedlings at 0, 8, 24, and 48 h following P0-mRFP induction revealed that AGO1 protein level decreases as the free-mRFP vacuolar degradation product of P0-mRFP accumulates (Fig. 1*E*), suggesting that P0-mRFP might be delivered to the vacuole along with its target AGO1. To address this, the pAGO1:GFP-AGO1/*ago1-27* transgenic line (29) was transformed with XVE:P0-mRFP, and lines harboring both constructs were analyzed. Imaging of root cells in the elongation zone following β-Es and ConcA treatment, compared to ConcA-only treated plants, revealed accumulation of P0-mRFP– and GFP-AGO1–containing bodies within the vacuoles (Fig. 1*F*). Time-lapse imaging demonstrated random motion of the bodies, which is typical for vacuole-lumen-residing autophagic bodies (Movie S3). Together, these observations point toward the ER as a major site from which P0 induces AGO1 degradation and from which it is delivered to the vacuole along with AGO1.

Autophagy Deficiency Impairs P0 Delivery to the Vacuole, yet Is Unable to Block AGO1 Degradation. Next, we examined whether P0 associates with autophagy components and whether it relies on autophagy for its function. We previously showed that GFP-AGO1 colocalizes with an autophagosome marker, mRFP-ATG8a, especially following *P0* expression or treatment with the membrane-permeable cysteine protease inhibitor E64d in *N. benthamiana* leaves (29). To determine whether P0 also colocalizes with autophagosomes, we coexpressed P0-GFP and mRFP-ATG8a in *N. benthamiana* leaves and imaged them at 40 hfa. As expected, the mRFP-ATG8a protein was detected in the cytosol and the nucleus, as well as in small bodies representing autophagosomes (Fig. 2*A*). Notably, P0-GFP predominantly colocalized with mRFP-ATG8a in these bodies. To determine whether the degradation of P0 bodies is regulated by autophagy, we introduced XVE:P0-mRFP or XVE:P0-myc into *atg5-1* and *atg7-2*, in which autophagy is inactive (49). First, we utilized XVE:P0-mRFP/*atg5-1* and XVE:P0-mRFP/*atg7*-2 lines and examined their vacuoles following 18- to 24-h P0-mRFP induction (β-Es) and treatment with ConcA. While P0-mRFP bodies accumulated in the vacuoles of control plants (XVE:P0-mRFP; on average exhibited 59 bodies per 1,000 μm^2 of vacuole lumen focal plane), there were almost no bodies detected in XVE:P0-mRFP/*atg5-1* (1 body per 1,000 μm^2) and significantly less P0-mRFP bodies (3.6 bodies per 1,000 μm^2) within the vacuoles of XVE:P0-mRFP/*atg7-2* (Fig. 2 *B* and *C*). Moreover, in cells of the meristematic zone, both autophagy mutants displayed cytosolic structures of about 4 μm in diameter that contain P0-mRFP and that were absent from wild-type cells (Fig. 2*B*). These structures were motile (Movie S4) and may represent aggregated P0-mRFP that accumulates due to degradation blockage.

Given this observation and the fact that the application of vacuolar-degradation inhibitors such as E64d is sufficient to counteract the degradative effect of P0-myc on AGO1 (29), we speculated that genetic disruption of autophagy might achieve similar results. To test this, we utilized our XVE:P0-myc/*atg5-1* and XVE:P0-myc/*atg7-2* lines and expressed P0-myc in 2 ways: 1) by germinating the plants on β-Es containing media (constitutive *P0* expression) compared to mock (DMSO containing media) or 2) by treating seedlings with β-Es or mock 5 d after their germination (induced *P0* expression). Strikingly, following P0 expression in both assays (Fig. 2*D* and *SI Appendix*, Fig. S5 *A* and *B*), none of the autophagy mutant was able to block either AGO1 or AGO2 degradation. On the contrary, the AGO1 transcript level was significantly increased, ruling out the possibility that the decline of protein level is due to reduced transcript level (Fig. 2*D*). Note that AGO1, but not AGO2, protein level remained stable in the *ago1-57* allele background, used here as a control. This line is insensitive to P0, as this mutation abrogates the SCF-dependent P0 interaction with AGO1 (46).

We next wondered whether the 26S proteasome could take over P0-mediated AGO1 protein decay if autophagy is compromised. However, when applying Bortezomib, which binds and blocks with high affinity and specificity the 26S proteasome (50), AGO1 was still degraded by P0 in *atg5-1* mutants, while the accumulation of the proteasome-sensitive transcription factor EIN3 (51) demonstrated the efficiency of the chemical (*SI Appendix*, Fig. S5 *C*, *Top*). Note that AGO1 transcript level was increased following P0 induction, ruling out, again, any negative effect on transcription to explain AGO1 decay (*SI Appendix*, Fig. S5 *C*, *Bottom*). From these experiments, we conclude that P0 can bypass autophagy deficiency to achieve a reduction in AGO1 protein level even when its delivery to the vacuole appears to rely on canonical autophagy.

P0 Is Engulfed by ATI1- and ATI2-Decorated Bodies on the ER and Is Delivered with Them to the Vacuole. To get insight into the P0 ER-to-vacuole delivery pathway, we decided to examine the possible involvement of the ER and autophagy-associated ATI1/2. We were particularly intrigued by the morphological resemblance (as seen in bright-field imaging) of the P0- and AGO1-containing bodies in the vacuole (*SI Appendix*, Fig. S6*A*) and cytosol (*SI Appendix*, Fig. S6*B*), with the ER-associated and ATI1-decorated bodies (ATI-bodies) reported earlier (42). ATI1/2 were shown to interact with ATG8 proteins and to be delivered on dynamic ER-derived ATI-bodies to the vacuole (42). To examine the possible involvement of ATI1/2 in the process of P0-mediated AGO1

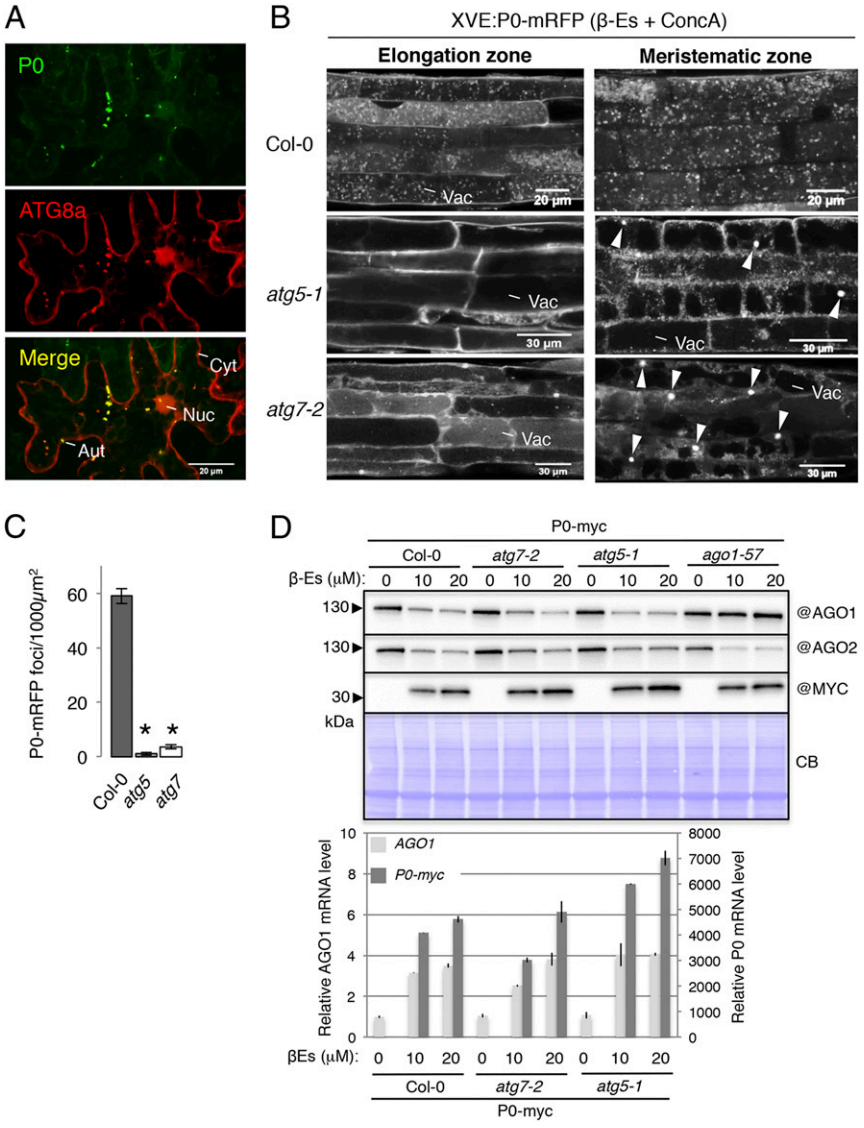

Fig. 2. Effects of autophagy deficiency on P0 flux to the vacuole and AGO1 degradation. (*A*) CLSM imaging of a tobacco leaf epidermal cell, transiently expressing P0-GFP (P0) and mRFP-ATG8a (ATG8a). A representative body that contains both P0 and ATG8a is designated as autophagosome (Aut). The nucleus (Nuc) and cytoplasm (Cyt) are marked as well. (*B*) CLSM imaging of cells in the (*Left*) root elongation zone and (*Right*) meristematic zone from *Arabidopsis* lines harboring XVE:P0-mRFP in the background of Col-0, *atg5-1*, and *atg7-2*, following treatment with β-Es and ConcA. Vacuole lumen (Vac) is indicated as well as large (~5 μm in diameter) cytosolic structures (arrowheads). (*C*) Quantification of the amount of P0-mRFP labeled autophagic bodies normalized to 1,000 μm^2 of vacuole lumen focal plane, in the background of the indicated genotypes. Plants were chosen for quantification based on their comparable P0-mRFP fluorescence intensity as detected from their cell's cytosol. Values represent mean ± SEM (n = 21, 30, and 23 elongation zone cells for *Col-0*, *atg5*, and *atg7* backgrounds, respectively); * denotes statistical significance of mutants compared to wild type, $P < 0.01$ (*t* test). (*D*) (*Top*) Immunoblot analysis of total proteins from XVE:P0-myc containing lines in the background of Col-0, *atg7-2*, *atg5-1*, and *ago1.57* seedlings that were germinated on 0, 10, or 20 μM of β-Es. Blots were probed with specific antibodies as indicated, and CB staining serves as loading control. (*Bottom*) Samples indicated in *Top* were also analyzed for AGO1 and P0 transcript levels by qRT-PCR. Values are average ± SD relative to P0-myc without β-Es.

decay, we first expressed ATI1-mCherry or ATI2-mCherry with P0-GFP in *N. benthamiana* leaf epidermal cells. Already at 30 hfa, we could detect the P0-GFP signal colocalizing with ATI1-mCherry labeled bodies (Fig. 3 *A*, *Top*) in a manner similar to P0 colocalization with ATG8a (Fig. 2*A*). Notably, at 120 hfa, the P0-GFP signal was detected engulfed by a ring-shaped ATI1-mCherry signal (Fig. 3 *A*, *Middle*), and, occasionally, structures reaching the size of 5 μm in diameter (Fig. 3 *A*, *Bottom*) were detected. Similar results were obtained when ATI2-mCherry was expressed with P0-GFP (*SI Appendix*, Fig. S7*A*). Moreover, we could also detect bodies within the vacuole lumen displaying both ATI1 and P0 signals in both epidermal (*SI Appendix*, Fig. S7*B*) and mesophyll cells (*SI Appendix*, Fig. S7*C*).

Next, we transformed *Arabidopsis* plants harboring ATI1-GFP under the regulation of the *ATI1* endogenous promoter [pATI1:ATI1-GFP (43)] with the XVE:P0-mRFP construct. Seedlings containing both markers were imaged following 18 h of treatment with β-Es and ConcA. Their vacuoles exhibited a large number of bodies, many of which appeared to be labeled with both P0-mRFP and ATI1-GFP proteins (Fig. 3*B*). Quantification of the relative abundance of each of the body types within vacuoles of P0-mRFP–expressing cells revealed that 80.5% of these bodies contained both proteins (yellow bar), 17% contained only ATI1-GFP (green bar), and 2.5% contained only P0-mRFP (red bar) (Fig. 3*C*). This indicates that the majority of the P0 cargo is delivered to the vacuole via ATI-bodies.

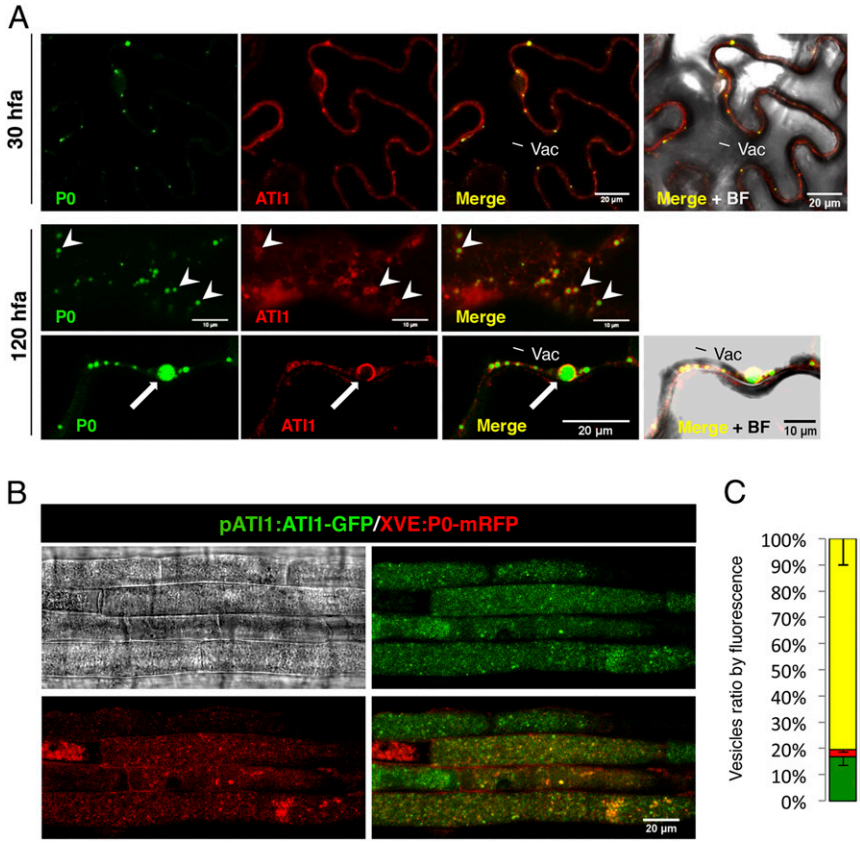

Fig. 3. ATI1 engulfs P0 on the ER, and both proteins are delivered to the vacuole. (*A*) *N. benthamiana* epidermal leaf cells transiently expressing P0-GFP and ATI1-mCherry were imaged by CLSM at (*Top*) 30 and (*Middle* and *Bottom*) 120 hfa. Arrowheads designate structures containing P0-GFP and surrounded by ATI1-mCherry ring-like shapes. White arrow marks a large (~5 μm in diameter) body. BF, bright field. (*B*) Cells in the root elongation zone of *Arabidopsis* seedlings harboring pATI1:ATI1-GFP and XVE:P0-mRFP, imaged following treatment with β-Es + ConcA. (*C*) Quantification of the relative number of bodies exhibiting only ATI1-GFP (green), only P0-mRFP (red), or both ATI1-GFP and P0-mRFP double labeling (yellow) out of the total number of bodies inside vacuoles. Values represent ratio means minus SEM ($n = 12$ plants) of data collected from a total of 51 cells in the elongation zone and normalized to 1,000 μm^2 of vacuole lumen focal plane.

P0 Induces the Flux of ATI-Bodies to the Vacuole. The accumulation of P0- and ATI1-labeled autophagic bodies in vacuoles suggests that P0 may induce an ER-derived degradation pathway involving ATI1. To investigate this possibility, we examined the response of the pATI1:ATI1-GFP/XVE:P0-mRFP transgenic line and its corresponding parental line that does not contain P0-mRFP (pATI1:ATI1-GFP) to β-Es and ConcA treatment. We reasoned that any change in the flux of ATI1-GFP bodies to the vacuole could be attributed solely to P0-mRFP expression. Confocal imaging revealed that, although there was a basal flux of ATI1-GFP bodies to the vacuoles in the parental line, there were significantly more bodies in the vacuoles of the plants expressing P0-RFP (Fig. 4*A*). Indeed, further quantification revealed a 5-fold increase in the number of vacuolar ATI1-GFP bodies in plants in which P0-RFP has been induced (Fig. 4*B*). Strikingly, this induction of ATI1-bodies was not accompanied by increased transcript nor protein levels of ATI1-GFP (Fig. 4*C*) as inferred from the examination of pATI1:ATI1-GFP/XVE:P0-mRFP and pATI1:ATI1-GFP seedlings grown on mock (DMSO) or 5, 10, and 20 μM β-Es. To investigate whether *P0* induction might show a broader effect on the transcript levels of autophagy-related genes, we analyzed the transcript level of *ATI1, ATI2, ATG8a, NBR1, ATG5, ATG2*, and *ATG7* in mock or 10 μM β–E–treated Col-0 or XVE:P0-myc plants. Despite a strong induction of P0-myc expression in the β–E–treated XVE:P0-myc plants, there was no significant change in the transcript of any of the tested genes (Fig. 4*D*). Together, these results suggest a posttranslational effect driven by P0 for the induction of the ATI degradation pathway.

ATI1 Interacts with AGO1 on the ER, and *ATI1/2* Deficiency Compromises Posttranscriptional Gene Silencing. Our results suggest that P0 induces the ATI degradation pathway, which may represent an endogenous pathway for the turnover of ER-bound AGO1. Therefore, we wondered whether ATI1/2 are involved in AGO1 regulation independently of P0. First, we expressed ATI1 fused to mCherry (ATI1-mCherry) with GFP-AGO1 transiently in *N. benthamiana* leaves to examine whether AGO1 and ATI1 are associated. Both proteins colocalized on the ER and also in ER-associated bodies, wherein ATI1 engulfed the GFP-AGO1 signal, forming a ring-like shape (Fig. 5*A*). As the ATI pathway is induced by starvation (42), we examined ATI1-GFP or GFP-AGO1 degradation kinetics in response to carbon and nitrogen deficiency (–C–N) by assessing the ratio of full-length proteins with free-GFP degradation products. Notably, the 2 proteins behaved similarly, where, at 24 h, degradation was initiated and subsequently increased following the onset of starvation (*SI Appendix*, Fig. S8 *A* and *B*). Yet comparing GFP-AGO1 starvation-mediated degradation with P0-induced degradation revealed a greater effect of starvation (*SI Appendix*, Fig. S8*C*). To evaluate ATI1 and AGO1 mutual dynamics during starvation, we generated transgenic lines harboring pAGO1:GFP-AGO1 and XVE:ATI1-mCherry in the *ago1-27* background. We then applied β-Es to induce ATI1- or ATI2-mCherry

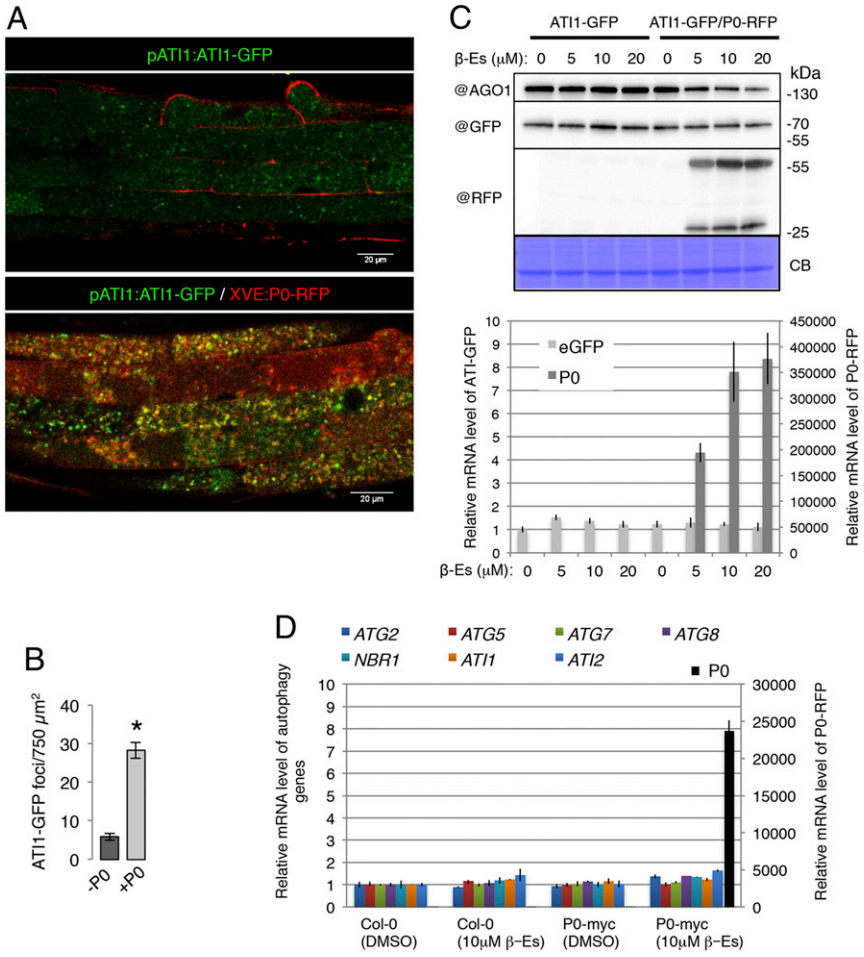

Fig. 4. P0 induces ATI1-labeled bodies flux to the vacuole without affecting ATI1 protein or transcript levels. (*A*) Cells in the root elongation zone of seedlings harboring pATI1:ATI1-GFP alone or pATI1:ATI1-GFP with XVE:P0-mRFP were treated with β-Es + ConcA for 16 h before vacuole focal planes were imaged with a CLSM. (*B*) Quantification of ATI1-GFP-labeled bodies per vacuole lumen area unit (750 µm^2) from pATI1:ATI1-GFP (–P0) or pATI1:ATI1-GFP/XVE:P0-mRFP (+P0). Values represent means ± SEM ($n > 30$). Statistical significance (*$P < 0.001$) was revealed by Student's *t* test. (*C*) Immunoblot analysis of total proteins from pATI1:ATI1-GFP alone or pATI1:ATI1-GFP/XVE:P0-mRFP seedlings germinated on 0 (DMSO), 5, 10, and 20 µM β-Es for 6 d. (*Top*) Blots were probed with specific antibodies as indicated (*Upper*). CB staining serves as loading control. (*Bottom*) Samples indicated in *Top* were also analyzed for AGO1 and ATI1-GFP transcript levels by qRT-PCR. Values are average ± SD relative to pATI1:ATI1-GFP without β-Es. (*D*) Relative transcript levels of selected autophagy-related genes (indicated) in Col-0 and XVE:P0-myc seedlings treated with either mock (DMSO) or 10 µM β-Es. Values are average ± SD relative to the corresponding gene expression in Col-0 treated with DMSO.

expression along with 24 h of darkness and 16 h of ConcA treatment. Confocal Laser Scanning Microscopy (CLSM) imaging of cells in the elongation zone revealed the accumulation of bodies within the vacuole lumen, most of which harbor both GFP-AGO1 and ATI1-mCherry (Fig. 5*B*), reminiscent of the colocalization of ATI1-GFP and P0-mRFP in the vacuole (Fig. 3*B*). Note that arrowheads in Fig. 5 *B*, *Inset* highlight ring-like shapes of ATI1-mCherry signal engulfing GFP-AGO1 signal, a morphology that is preserved up to the vacuole.

These observations prompted us to examine whether ATI1/2 could directly interact with AGO1. We first used a yeast 2-hybrid approach. Due to problems of expression of the full-length AGO1 protein in this system, we examined separately the AGO1 N-terminal half extending from the PolyQ to the PAZ domain and the C-terminal half (L2-Ct) (Fig. 5*C*). In this system, AGO1 interacted with ATI1 and ATI2, although less strongly than with ATG8a used here as a control (Fig. 5*C*). This was especially evident for the interaction of ATI1 with the AGO1 PolyQ-PAZ N-terminal half. To validate the interactions *in planta*, we also performed Bimolecular Fluorescence Complementation (BiFC) assays (*SI Appendix*, Fig. S9). Thus, we generated BiFC construct combinations and tested them in agroinfiltrated tobacco leaves. We found that AGO1 interacted with ATI1 in cellular structures exhibiting an expression pattern that resembles the pattern generated by the combination of ATI1 and ATG8a. However, AGO1 combined with the empty vectors or with ATG8a did not produce such fluorescence (*SI Appendix*, Fig. S9*A*). Next, *N. benthamiana* infiltrated leaf patches were further treated with ConcA in the dark for 16 h. Under these condition, bodies emitting YFP fluorescence within vacuoles were detected when ATI1 was combined with AGO1 or ATG8a (*SI Appendix*, Fig. S9*B*, white arrowheads), but not when coexpressed with FBW2, an F-box protein that was previously suggested to be associated with AGO1 (52). This confirms that ATI1–AGO1 interaction is preserved up to the vacuole (*SI Appendix*, Fig. S9*B*). To evaluate whether this association is detected also in *Arabidopsis*, we further performed coimmunoprecipitation (Co-IP) assays of AGO1 from 35S:ATI1-GFP expressing plants. As control, we used the *Arabidopsis* pKAO2:KAO2-GFP line expressing an ER-associated ent-kaurenoic acid oxidase 2 (KAO2), a gibberellin biosynthesis enzyme fused to GFP (53), showing an expression level comparable to ATI1-GFP. Indeed,

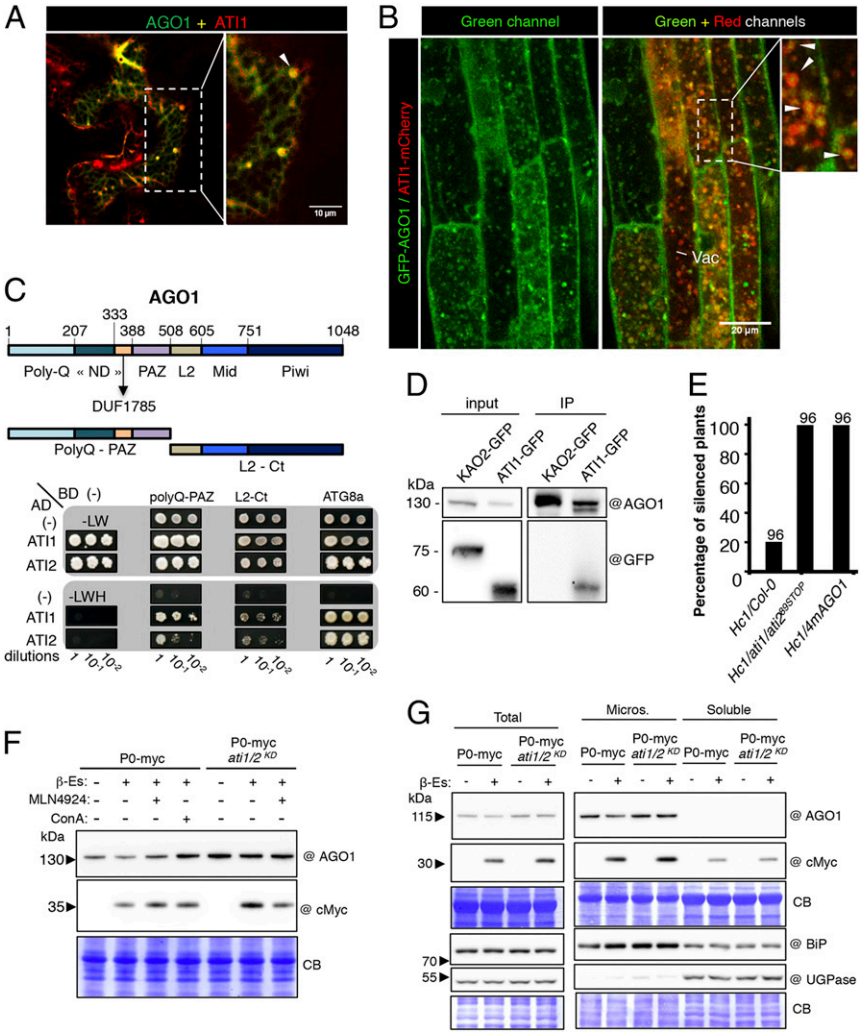

Fig. 5. ATI1 associates with AGO1 on the ER and in the vacuole independently of P0, and ATI1/2 are required for S-PTGS. (*A*) (*Left*) CLSM imaging of a tobacco leaf epidermal cell transiently expressing GFP-AGO1 and ATI1-mCherry. (*Right*) A magnification of the area indicated by a dashed line in *Left*. The arrowhead highlights a representative spherical structure labeled with ATI1-mCherry and enriched with GFP-AGO1 signal. (*B*) Transgenic *ago1-27* seedlings expressing pAGO1:GFP-AGO1 and XVE:ATI1-mCherry were treated with both β-Es and ConcA, and the vacuolar focal plane of cells in the root elongation zone was imaged by a CLSM. Magnification of the area indicated by a dashed line is presented, with arrowheads highlighting spherical structures exhibiting ATI1-mCherry engulfing GFP-AGO1 signal. (*C*) Y2H-assay for interaction analysis of ATI1 or ATI2 with either the N-terminal (PolyQ-PAZ) or C-terminal (L2-Ct) halves of AGO1. (*Top*) A scheme illustrating the PolyQ-PAZ (N-terminal) and L2-Ct (C-terminal) fragments of AGO1 and their amino acid coordinates. (*Bottom*) Yeast cells expressing ATI1 or ATI2 as AD fusion and PolyQ-PAZ or L2-Ct as BD fusion show growth on selective medium, without leucine and tryptophan (–LW) or leucine, tryptophan, and histidine (–LWH). Combinations with empty BD or AD vectors (–) are also shown. Interactions of ATI1 or ATI2 with ATG8a serve as a positive control. Yeast cells representing all combinations were plated directly or following 10- or 100-fold dilutions. (*D*) Co-IP analysis of AGO1 from crude protein extracts of 35S:ATI1-GFP or pKAO2:KAO2-GFP plants, performed with beads conjugated to @AGO1 antibodies. Input and IP fractions were immunoblotted with @AGO1 and @GFP (JL8) antibodies. (*E*) S-PTGS efficiency in the indicated genotypes. GUS activity was measured in leaves of 50-d-old plants. For each genotype, 96 plants were analyzed. S-PTGS efficiency is expressed as the percentage of GUS-negative plants. (*F*) Immunoblot analysis of total protein from 10-d-old XVE:P0-myc and XVE:P0-myc/*ati1ati2*^{KD} seedlings grown on MS plate, then treated as indicated. For treatment, the seedlings were transferred to liquid MS containing DMSO (Mock treatment), β-Es (10 µM), MLN4924 (25 µM), or ConcA (1 µM) in the indicated combinations and left in the growth chamber with mild steering for 24 h. Blots were probed with antibodies raised against *Arabidopsis* AGO1 and the c-MYC tag. CB staining serves as loading control. (*G*) Immunoblot analysis of total, microsomal pellet (Micros.), and supernatant (Soluble) protein preparations from XVE:P0-myc and XVE:P0-myc/*ati1ati2*^{KD} 6-d-old seedlings grown on MS plates, then treated as indicated; 1/2 MS liquid media containing either DMSO (–) or 20 µM β-Es (+) was added directly on vertically growing seedlings for 24 h before protein extraction. Blots were probed with antibodies raised against *Arabidopsis* AGO1, the c-MYC tag (top membrane), luminal binding proteins BiP1/BiP2/BiP3 (BiP), and UGPase (bottom membrane). CB staining on both membranes serves as loading control.

immunoprecipitation of AGO1 coprecipitated ATI1-GFP, but not KAO2-GFP (Fig. 5*D*).

We consequently examined the steady-state level of AGO1 protein in *ATI1/2*-deficient plants. The already reported SAIL_404_D09 line (*ati1*) was used, either as a single mutant or combined with an RNAi construct that reduces *ATI2* expression by 80% (42) (*SI Appendix*, Fig. S10*A*), which we termed *ati1ati2*^{KD}. In addition, we applied the CRISPR-Cas9 approach to target *ATI2* in the background of the *ati1* mutant line. This yielded a 5-base pair (bp) deletion in *ATI2* that resulted in a frameshift generating an early stop codon after the new codon number 88 (*SI Appendix*, Fig. S10*B*). This double mutant was named *ati1ati2*^{STOP}. Similar to *ati1ati2*^{KD}, the *ati1ati2*^{STOP} mutant was viable and did not exhibit visible developmental alterations in our growing conditions (*SI Appendix*, Fig. S10*C*). In all *ati1/2* mutants, as well as in *atg5-1*, we observed a mild increase in

AGO1 protein steady-state levels as compared to Col-0 (*SI Appendix*, Fig. S10*D*).

Finally, we investigated whether *ATI1/2* loss of function affects AGO1-based silencing activity. For this purpose, we used the Hc1 silencing reporter line (54) that triggers AGO1-dependent S-PTGS in only 20% of the population at each generation (54) and thus represents an excellent sensor to precisely monitor changes in silencing efficiency (55). In particular, it was shown previously that expressing an miR168-resistant form of the AGO1 mRNA in this line increases S-PTGS efficiency up to 100%, indicating that the amount of AGO1 protein available for S-PTGS is limiting in wild-type plants (56). While, as expected, about 20% of silencing was observed in the Col-0 background, 100% of the *Hc1/ati1ati2*^{STOP} plants were silenced (Fig. 5*E*), similar to the *Hc1/4mAGO1* plants that were used as a control. From these results, we conclude that, while *ATI1/2* deficiency has only a minor effect on total AGO1 steady-state protein level, it significantly enhances S-PTGS, likely by increasing the availability of AGO1 for S-PTGS.

***ATI1/2* Deficiency Attenuates P0-Mediated Decay of Membrane-Associated AGO1.** Next, we investigated whether P0-mediated AGO1 protein degradation is affected in *ATI1/2*-deficient plants. Thus, the XVE:P0-myc line was crossed with the *ati1ati2*^{KD} mutant line. Interestingly, when we induced P0-myc expression for a short period (treating seedlings with β-Es or mock for 24 h), AGO1 degradation was attenuated in the *ati1ati2*^{KD} mutant background, despite a higher expression level of P0-myc (Fig. 5*F*). To get further insight into this process, we performed microsomal preparations from XVE:P0-myc seedlings in Col-0 and *ati1ati2*^{KD} backgrounds that were subjected, or not, to 24 h of β-Es to induce P0-myc. Western-blot with anti-AGO1 antibodies revealed decreased AGO1 level in the total protein fraction in the Col-0 background relative to the *ati1/2* mutant background (Fig. 5*G*). As most AGO1 protein was found in the microsomal fraction, its impaired degradation in this fraction suggests that ATI1/2 are required especially for membrane-bound AGO1 degradation via P0. However, this effect was not observed when seedlings were treated with β-Es or mock for 7 d after their germination (*SI Appendix*, Fig. S11), indicating that long-term induction leading to higher level of P0 expression is able to overcome the absence of ATI1/2 and likely proceed with AGO1 degradation through an unrelated degradation pathway.

Discussion

The Route for P0-Mediated ER-To-Vacuole Delivery of AGO1. Several studies in different organisms and cell types indicate that AGO proteins display multiple intracellular localizations (reviewed in refs. 57 and 58). Thus, AGOs could be detected as soluble proteins in the cytosol and nucleus, as part of a dense complex of macromolecules termed P-bodies, in foci termed siRNA-bodies or stress granules, and, at least, human AGO2 was also reported to be associated with multivesicular bodies (MVBs) and even mitochondria. In plants, reporter lines expressing functional GFP-AGO1 argue for cytosolic distribution for most of the protein, at least in root cells (29, 59). Nonetheless, a significant pool of AGO1 protein was found membrane-bound (13, 47), where the RISC appears to exert its translation repression activity. Intriguingly, miRNA RISCs are not only present in membrane-bound polysomes, but they can trigger there secondary siRNA production from both coding and noncoding RNA (48). These results suggest that both the translation repression and the endonuclease functions of AGO1 may occur on the ER. This is not unique to plants, as translation repression by a special type of ER-associated RISC was also reported in *Drosophila* cells, especially following starvation (60), and the outer rough ER membrane was suggested as the site of human Ago2 loading with siRNA and of mRNA slicing (61). Our live-cell imaging and immuno-EM approaches further support the ER localization of AGO1, although it might also localize to other membranes such as the plasma membrane. Notably, treatment with β-Es and ConcA resulted in a significant enrichment of AGO1 along the ER. As ConcA inhibits cellular trafficking and autophagy, it is likely that the ER represents the major site from which AGO1 is sent to the vacuole for degradation under normal growing conditions.

This strong enrichment of AGO1 on the ER raises the question of where, at the subcellular level, does P0 encounter AGO1 to trigger its degradation. The nucleus would have been a site of choice, as numerous F-box proteins target their substrates in this compartment (62). Moreover, AGO1 loading by at least miRNAs is likely to be nuclear (59). Therefore, AGO1 conformational changes in this compartment might favor the recognition of its P0 degron (46). In addition, autophagy-mediated degradation of *Arabidopsis* nuclear-localized proteins and even protein complexes was already demonstrated (41, 63). However, our data point to the ER as the main site where P0 interacts with AGO1. Likely, P0 interacting with AGO1 on the ER induces a flux of bodies containing both the F-box and its target, which are subsequently degraded in the vacuole (Fig. 1*F*). Interestingly, these bodies resembled ATI1/2 spherical bodies that were shown to be involved in direct ER-to-vacuole trafficking under carbon starvation (42).

ATI1/2 Deficiency Displays a Mild Effect on Total AGO1 Protein Level, yet a Significant Effect on Its Function. ATI1/2 were previously detected localized in ER membranes and in dark-induced ER-associated bodies that eventually reach the vacuole (42). Nevertheless, the identities of potential ER-localized cargos carried via the ATI1/2 pathway were so far unknown. If AGO1 would be a cargo of this pathway, one could hypothesize that the loss of ATI1/2 function may affect AGO1 stability or activity. Regarding its stability, the analysis of single and double *ati1/2* mutants showed no major increase of AGO1 protein steady-state level in total extracts when compared to Col-0 (*SI Appendix*, Fig. S10*D*). Also, similarly to *atg5* and *atg7*, the *ati1/2* mutant did not prevent AGO1 degradation following long and constitutive expression of P0 (*SI Appendix*, Fig. S11 and Fig. 2*D*). However, *ATI1/2* deficiency led to increased stability of AGO1 when P0 was induced for a relatively short duration, an effect that was prominent in microsomal preparations (Fig. 5 *F* and *G*). This may be the result of a more profound effect of P0 on the ER in initial time points, whereas, during long overexpression, P0 may exert its function in other subcellular locations of AGO1, in which ATI1/2 might not be involved. Note that AGO1 protein accumulation in *ati1/2, atg5*, and *atg7* mutant backgrounds might be attenuated by miR168-dependent feedback loop regulating AGO1 expression (64), and possibly also by an alternative route for AGO1 decay (discussed below). Another possible explanation for the mild effect of ATI1/2 on AGO1 level is the existence of additional, yet unknown, autophagy receptors that target AGO1 or other RISC components that might function cooperatively with ATI1/2 for AGO1 degradation. This idea gains support from a recent study that compared the function of mammalian ER-phagy receptors (65). This work revealed that deficiency in 4 out of 5 known ER-phagy receptors did not fully abolish ER-phagy activity and that the 3 major receptors (TEX264, CCPG1, and FAM134B) act cooperatively to execute ER-phagy. Therefore ATI1/2 may serve as ER-phagy receptors whose function is induced upon P0 expression to carry ER fragments to the vacuole along with associated molecules. Interestingly, ATI1/2 were recently reported to interact with ATG8 via their intrinsically disordered regions that harbor the ATG8-Interacting Motif domains (66), a feature that seems to be common among ER-phagy receptors (65). Yet, even under such a scenario, some degree of specificity toward AGO1 is certain, as demonstrated by

ATI1–AGO1 binding and their codelivery to the vacuole while remaining bound (Fig. 5 *C* and *D* and *SI Appendix*, Fig. S9).

Finally, the significant effect of *ATI1/2* deficiency on AGO1 function further supports the role of this pathway in selective targeting of AGO1. Thus, the *ati1ati2*^{STOP} mutant increased significantly S-PTGS efficiency of the *Hc1* line, indicating that ATI1/2 limits S-PTGS efficiency. Because AGO1 is a limiting factor for PTGS (56), we speculate that the lack of *ATI1/2* might increase AGO1 activity at specific locations (e.g., the ER) that subsequently could increase S-PTGS efficiency.

Does the Loading of AGO1 by sRNAs Affect the Degradation by P0? It has previously been proposed that P0 triggers the clearance of unloaded AGO1 (24). However, this does not seem consistent with the association of P0 with the ER-localized pool of AGO1, presumably in an active and loaded form. This is further supported by the facts that 1) P0 reduces the amount of miRNAs and siRNAs in microsomal fractions (*SI Appendix*, Fig. S1) and 2) P0 induces the ER-derived ATI pathway, which apparently limits S-PTGS activity. The discrepancy between our observations and the report of Csorba et al. (24) may be explained by the fact that their experiments were conducted with transient overexpression assays. This approach may result in the disruption of the balance between the nuclear and cytosolic pools of AGO1 (59). That being said, the efficiency of P0 in degrading AGO1 and other AGO proteins suggests that P0 could function in several compartments and probably on several forms of AGO1. This idea gains support from the observation that AGO1 is efficiently degraded in both the microsomal and soluble fractions and that AGO4, which is exclusively soluble (48) and mainly localized in the nucleus, is efficiently degraded by P0 (Fig. 1*A*).

Autophagy Is Not the Only Pathway for P0-Mediated AGO1 Decay. One unexpected and intriguing observation of our work is the inability of autophagy deficiency to block P0-mediated degradation of AGO1 (Fig. 2*D*), especially because general inhibitors that interfere with trafficking pathways and block vacuolar degradation prevented the AGO1 decay pathway (29). Moreover, while P0-mediated degradation of membranous AGO1 was attenuated in the *ati1ati2*^{KD} mutant (Fig. 5 *F* and *G*), long-term induction of P0 still led to AGO1 protein decay (*SI Appendix*, Fig. S11). Therefore, it is possible that P0 channels AGO1 for degradation via autophagy as well as via an autophagy-independent pathway, either generally or specifically when autophagy is blocked. It is known that cargos are sent to the vacuole also via MVBs (67, 68); however, no significant association with MVBs was previously observed for GFP-AGO1 (29). Notably, alternative routes of autophagy, such as Atg5/Atg7-independent macroautophagy, have been reported in mammals (69), but their function and mechanisms are still not well understood.

The human Ago2 protein can be degraded in a proteasome-dependent manner (70). Alternatively, human Ago2 was also been found associated with the nuclear dot protein 52 (NDP52), which is a cargo receptor for autophagy (71). We therefore investigated whether the 26S proteasome may mediate AGO1 decay if autophagy was impaired, but this was also not the case (*SI Appendix*, Fig. S5*C*). However, as a functional F-box domain is essential for the assembly of SCF^{P0}, its interaction with AGO1 and its subsequent degradation (46), it is likely that the ubiquitylation of AGO1 or a protein associated with AGO1 triggers these degradation pathways. Therefore, we conclude that conventional autophagy is not the only route for P0-mediated AGO1 degradation in plant cells and further research is required to reveal additional pathways.

Proviral and Antiviral Functions of Autophagy. The pivotal role of autophagy during viral infection in plants has only recently emerged with reports demonstrating both antiviral and proviral functions (44, 45). Thus, in *Arabidopsis*, the autophagy receptor NBR1 was shown to limit cauliflower mosaic virus infection via targeting of viral capsid proteins and particles for degradation (39). Similarly, ATG8F from tobacco and tomato interacts with the virulence factor βC1 of Cotton leaf curl Multan virus (72) and tobacco Beclin1 interacts with turnip mosaic virus (TuMV) RNA-dependent RNA polymerase (73), leading to the degradation of the viral proteins via autophagy and thus limiting the corresponding viral infections. In contrast to these antiviral functions, viruses also manipulate autophagy for their benefits. Thus, TuMV can suppress NBR1-mediated selective autophagy of the VSR HcPro (74), whereas VPg, a VSR from the same virus, was shown to induce both autophagy and proteasomal degradation of the host antiviral silencing component, SGS3 (75). Most of these reports also demonstrated that viral infections were accompanied by autophagy induction. This was shown by the elevation of both the protein and transcript levels of *ATG* genes, as well as the accumulation of ATG8-labeled structures (39, 72, 75). However, viral components inducing autophagy are not well known.

Here we show that a single viral protein is sufficient to induce a specialized degradation pathway that originates from the ER. Notably, P0 did not result in the elevation of ATI1-GFP protein or gene expression (Fig. 4*C*), nor did it result in the increased expression of other autophagy-related genes (Fig. 4*D*). Hence, while autophagy induction may represent a global response to viral infection, some viral proteins may act in a more specialized manner to induce specific degradation pathways, likely for the benefit of the infection. Therefore, it is possible that, by merely the physical association of P0 with AGO1, the autophagy machinery is recruited to their interaction sites and delivers both proteins to the vacuole. According to such a scenario, P0 would act as a suicidal protein that is sacrificed by the virus to eliminate antiviral AGO proteins.

Materials and Methods

Plant Material, Growth Conditions, and Treatments with Chemicals. *Arabidopsis* ecotype Colombia as well as *N. benthamiana* (for transient expressions) were used in this study. *Arabidopsis* mutants *atg5-1*, *atg7-2*, *ati1ati2*^{KD}, and *ago1-57* (38, 42, 46) and the pAGO1:GFP-AGO1/*ago1.27* (29), 35S:ATI1-GFP (42), pATI1:ATI1-GFP (43), and pKAO2:KAO2-GFP (53) transgenic lines were previously described. For P0 expression, β-Es–responsive transgenic lines were obtained following floral dipping of Col-0, *atg5-1*, *atg7-2*, and pATI1:ATI1-GFP with *Agrobacterium tumefaciens* harboring XVE:P0-mRFP. The pAGO1:GFP-AGO1/*ago1-27* was floral-dipped with agrobacteria harboring XVE:P0-mRFP or XVE:ATI1-mCherry. Different genotypes were crossed to generate *atg7-2*/XVE:P0-myc and *atg5-1*/XVE:P0-myc. The list of primers used for genotyping is presented in Dataset S1.

The *Arabidopsis ati1ati2*^{STOP} mutant line was generated by floral-dipping–mediated transformation (Agrobacterium strain GV3101 pMP90) of *ati1* (SAIL_404_D09) mutant plants with the CRISPR construct described below. Hygromycin-resistant plants were sequenced, and one plant containing a 5-bp deletion in the *ATI2* gene sequence was chosen. Cas9-free (hygromycin sensitive) plants were then selected from a T3 population and confirmed by PCR and sequencing using primer ATI2Crisp_F and ATI2Crispr_R (Dataset S1) and used for further analysis.

For β-Es–mediated protein induction and chemical treatments, seeds were germinated on solid half-strength MS (pH 5.8) containing 1% sucrose (0.5 MS/suc) within 6-well plates that were positioned vertically. Five days following transfer to the growth room, 1 mL of liquid 0.5 MS/suc containing the indicated β-Es concentrations, with or without ConcA (1 μM), was applied in each well before imaging or protein/RNA extractions were conducted. Similar treatments with the appropriate amount of DMSO served as mock. Alternatively, seedlings were grown on horizontal MS containing 1% sucrose and then transferred to liquid MS medium containing the indicated drugs (β-Es, MLN4924, ConcA) for the indicated duration. For long-term induction, seedlings were germinated on solid half-strength MS media containing β-Es at the indicated concentrations (2, 5, 10, or 20 μM). Dark-induced starvation was applied as previously described (43). Unless otherwise specified, plants were grown under a 16 h light/8 h dark diurnal regime (long day). Chemicals are listed in Dataset S2.

Plasmid Construction. To generate XVE:ATI1-mCherry, the ATI1-mCherry coding sequence was amplified from established plasmids (42, 43) with flanking attB

sites (Dataset S1) and introduced into the pDON221 Vector (ThermoFisher). Note that the ATI1 coding sequence (CDS) contains a T348C silent mutation. Then, the gateway system was used to introduce the fused genes to pMDC7 vectors already harboring the β-Es–inducible system (76).

To generate 35S:GFP-AGO1, AGO1 CDS was amplified using primer attB1_AGO1_ F and attB2_AGO1_R (Dataset S1) and first mobilized into pDNR221. Then a second recombination using LRclonaseII was used to transfer AGO1 CDS into pB7WGF2.

To generate the pGADT7-ATI1, pGADT7-ATI2, and pGBKT7-ATG8a for expression in yeast, the coding sequences of all 3 proteins were first amplified from previously described plasmids (29, 42, 43) from ATG to stop codon (Dataset S1) and mobilized into the pDONR/Zeo Vector (ThermoFisher) via BPclonase II reaction. N-terminal and C-terminal parts of AGO1, respectively called polyQ-PAZ (Met1 to Glu501 of AGO1 CDS) and L2-Ct (Gly502 to Cys1048 of AGO1 CDS), were amplified using primers attB1_PolyQ-PAZ(AGO1)_F/attB2_PolyQ-PAZ(AGO1)_R and attB1_L2-Ct(AGO1)_F/attB2_L2-Ct(AGO1)_R (Dataset S1) and mobilized into pDONR/Zeo Vector using BP clonase II reaction. Then, the gateway system was used to introduce the different sequences into either the pGADT7-GW (AD) or the pGBKT7-GW (BD) destination vectors via LRclonase II reaction.

P0 and P0^{LP} were cloned from existing P0 clones into the pENTRY vector with attB sites (Dataset S1) and further mobilized using the GatewayTM technology into pH7RWG2, pK7FWG2, and pER8GWR to generate 35S:P0-mRFP, 35S:P0-GFP, and XVE:P0-mRFP and XVE:P0^{LP}-mRFP, respectively. The pER8GWR was generated by introducing the ccdB-RFP cassette from pH7RWG2.0 (SacII-SpeI fragment treated with mung bean nuclease followed by a treatment with DNA polymerase Klenow fragment) into the XhoI site of the pER8 vector (76) treated with the DNA polymerase Klenow fragment.

The CRISPR construct was built using the GoldenBraid cloning system (77) in pCAMBIA binary vectors. The Cas9 construct had been codon-optimized for expression in *Arabidopsis* plants under the regulation of a *UBI10* promoter (78). Target-binding sequences were cloned into the *Bbs*I sites of the U6-26:gRNA pGREEN vector as a T4 Polynucleotide Kinase-treated complementary-annealed oligonucleotide. For primers, see Dataset S1.

For BiFC assay-related plasmids, pENTRY clones harboring the CDS of ATI1, ATG8a, AGO1, and FBW2 were recombined to BiFC-compatible destination vectors pYFPN43 or pYFPC43 using the Gateway recombination cloning system. For primers, see Dataset S1.

ACKNOWLEDGMENTS. We acknowledge Dr. Jerome Mutterer for designing the ImageJ macro "2CH_bar"; Dr. Shdema Filler-Hayut and Prof. Avraham A. Levy for providing the CRISPR vector cassettes; Dr. Patrick Achard for the pKAO2:KAO2-GFP line; Dr. H. Eisler for the production of the EIN3 antibody; and Dr. Hadas Peled-Zehavi for helpful scientific discussions.

1. M. Ghildiyal, P. D. Zamore, Small silencing RNAs: An expanding universe. *Nat. Rev. Genet.* **10**, 94–108 (2009).
2. G. Meister, Argonaute proteins: Functional insights and emerging roles. *Nat. Rev. Genet.* **14**, 447–459 (2013).
3. C. Poulsen, H. Vaucheret, P. Brodersen, Lessons on RNA silencing mechanisms in plants from eukaryotic argonaute structures. *Plant Cell* **25**, 22–37 (2013).
4. J. Krol, I. Loedige, W. Filipowicz, The widespread regulation of microRNA biogenesis, function and decay. *Nat. Rev. Genet.* **11**, 597–610 (2010).
5. M. J. Axtell, Classification and comparison of small RNAs from plants. *Annu. Rev. Plant Biol.* **64**, 137–159 (2013).
6. A. K. L. Leung, P. A. Sharp, MicroRNA functions in stress responses. *Mol. Cell* **40**, 205–215 (2010).
7. S. W. Ding, RNA-based antiviral immunity. *Nat. Rev. Immunol.* **10**, 632–644 (2010).
8. A. Mussabekova, L. Daeffler, J. L. Imler, Innate and intrinsic antiviral immunity in *Drosophila*. *Cell. Mol. Life Sci.* **74**, 2039–2054 (2017).
9. H. Vaucheret, Plant ARGONAUTES. *Trends Plant Sci.* **13**, 350–358 (2008).
10. S. Mi *et al*., Sorting of small RNAs into *Arabidopsis* argonaute complexes is directed by the 5′ terminal nucleotide. *Cell* **133**, 116–127 (2008).
11. N. Baumberger, D. C. Baulcombe, *Arabidopsis* ARGONAUTE1 is an RNA Slicer that selectively recruits microRNAs and short interfering RNAs. *Proc. Natl. Acad. Sci. U.S.A.* **102**, 11928–11933 (2005).
12. P. Brodersen *et al*., Widespread translational inhibition by plant miRNAs and siRNAs. *Science* **320**, 1185–1190 (2008).
13. S. Li *et al*., MicroRNAs inhibit the translation of target mRNAs on the endoplasmic reticulum in *Arabidopsis*. *Cell* **153**, 562–574 (2013).
14. J. T. Cuperus *et al*., Unique functionality of 22-nt miRNAs in triggering RDR6-dependent siRNA biogenesis from target transcripts in *Arabidopsis*. *Nat. Struct. Mol. Biol.* **17**, 997–1003 (2010).
15. Q. Fei, R. Xia, B. C. Meyers, Phased, secondary, small interfering RNAs in post-transcriptional regulatory networks. *Plant Cell* **25**, 2400–2415 (2013).
16. F. Borges, R. A. Martienssen, The expanding world of small RNAs in plants. *Nat. Rev. Mol. Cell Biol.* **16**, 727–741 (2015).
17. J. B. Morel *et al*., Fertile hypomorphic ARGONAUTE (ago1) mutants impaired in post-transcriptional gene silencing and virus resistance. *Plant Cell* **14**, 629–639 (2002).
18. J. Azevedo *et al*., Argonaute quenching and global changes in Dicer homeostasis caused by a pathogen-encoded GW repeat protein. *Genes Dev.* **24**, 904–915 (2010).
19. N. Pumplin, O. Voinnet, RNA silencing suppression by plant pathogens: Defence, counter-defence and counter-counter-defence. *Nat. Rev. Microbiol.* **11**, 745–760 (2013).
20. T. Csorba, L. Kontra, J. Burgyán, Viral silencing suppressors: Tools forged to fine-tune host-pathogen coexistence. *Virology* **479-480**, 85–103 (2015).
21. M. Pazhouhandeh *et al*., F-box-like domain in the polerovirus protein P0 is required for silencing suppressor function. *Proc. Natl. Acad. Sci. U.S.A.* **103**, 1994–1999 (2006).
22. N. Baumberger, C. H. Tsai, M. Lie, E. Havecker, D. C. Baulcombe, The Polerovirus silencing suppressor P0 targets ARGONAUTE proteins for degradation. *Curr. Biol.* **17**, 1609–1614 (2007).
23. D. Bortolamiol, M. Pazhouhandeh, K. Marrocco, P. Genschik, V. Ziegler-Graff, The Polerovirus F box protein P0 targets ARGONAUTE1 to suppress RNA silencing. *Curr. Biol.* **17**, 1615–1621 (2007).
24. T. Csorba, R. Lózsa, G. Hutvágner, J. Burgyán, Polerovirus protein P0 prevents the assembly of small RNA-containing RISC complexes and leads to degradation of ARGONAUTE1. *Plant J.* **62**, 463–472 (2010).
25. A. F. Fusaro *et al*., The Enamovirus P0 protein is a silencing suppressor which inhibits local and systemic RNA silencing through AGO1 degradation. *Virology* **426**, 178–187 (2012).
26. R. S. Cascardo *et al*., Function and diversity of P0 proteins among cotton leafroll dwarf virus isolates. *Virol. J.* **12**, 123 (2015).
27. M. D. Petroski, R. J. Deshaies, Function and regulation of cullin-RING ubiquitin ligases. *Nat. Rev. Mol. Cell Biol.* **6**, 9–20 (2005).
28. Z. Hua, R. D. Vierstra, The cullin-RING ubiquitin-protein ligases. *Annu. Rev. Plant Biol.* **62**, 299–334 (2011).
29. B. Derrien *et al*., Degradation of the antiviral component ARGONAUTE1 by the autophagy pathway. *Proc. Natl. Acad. Sci. U.S.A.* **109**, 15942–15946 (2012).
30. N. Mizushima, B. Levine, A. M. Cuervo, D. J. Klionsky, Autophagy fights disease through cellular self-digestion. *Nature* **451**, 1069–1075 (2008).
31. G. Kroemer, G. Mariño, B. Levine, Autophagy and the integrated stress response. *Mol. Cell* **40**, 280–293 (2010).
32. S. Kaushik *et al*., Chaperone-mediated autophagy at a glance. *J. Cell Sci.* **124**, 495–499 (2011).
33. N. Mizushima, T. Yoshimori, Y. Ohsumi, The role of Atg proteins in autophagosome formation. *Annu. Rev. Cell Dev. Biol.* **27**, 107–132 (2011).
34. R. S. Marshall, R. D. Vierstra, Autophagy: The master of bulk and selective recycling. *Annu. Rev. Plant Biol.* **69**, 173–208 (2018).
35. V. Rogov, V. Dötsch, T. Johansen, V. Kirkin, Interactions between autophagy receptors and ubiquitin-like proteins form the molecular basis for selective autophagy. *Mol. Cell* **53**, 167–178 (2014).
36. A. Khaminets, C. Behl, I. Dikic, Ubiquitin-dependent and independent signals in selective autophagy. *Trends Cell Biol.* **26**, 6–16 (2016).
37. S. Svenning, T. Lamark, K. Krause, T. Johansen, Plant NBR1 is a selective autophagy substrate and a functional hybrid of the mammalian autophagic adapters NBR1 and p62/SQSTM1. *Autophagy* **7**, 993–1010 (2011).
38. J. Zhou *et al*., NBR1-mediated selective autophagy targets insoluble ubiquitinated protein aggregates in plant stress responses. *PLoS Genet.* **9**, e1003196 (2013).
39. A. Hafrén *et al*., Selective autophagy limits cauliflower mosaic virus infection by NBR1-mediated targeting of viral capsid protein and particles. *Proc. Natl. Acad. Sci. U.S.A.* **114**, E2026–E2035 (2017).
40. C. Hachez *et al*., The *Arabidopsis* abiotic stress-induced TSPO-related protein reduces cell-surface expression of the aquaporin PIP2;7 through protein-protein interactions and autophagic degradation. *Plant Cell* **26**, 4974–4990 (2014).
41. R. S. Marshall, F. Li, D. C. Gemperline, A. J. Book, R. D. Vierstra, Autophagic degradation of the 26S proteasome is mediated by the dual ATG8/ubiquitin receptor RPN10 in *Arabidopsis*. *Mol. Cell* **58**, 1053–1066 (2015).
42. A. Honig, T. Avin-Wittenberg, S. Ufaz, G. Galili, A new type of compartment, defined by plant-specific Atg8-interacting proteins, is induced upon exposure of *Arabidopsis* plants to carbon starvation. *Plant Cell* **24**, 288–303 (2012).
43. S. Michaeli, A. Honig, H. Levanony, H. Peled-Zehavi, G. Galili, *Arabidopsis* ATG8-INTERACTING PROTEIN1 is involved in autophagy-dependent vesicular trafficking of plastid proteins to the vacuole. *Plant Cell* **26**, 4084–4101 (2014).
44. M. Clavel, S. Michaeli, P. Genschik, Autophagy: A double-edged sword to fight plant viruses. *Trends Plant Sci.* **22**, 646–648 (2017).
45. D. Hofius, L. Li, A. Hafrén, N. S. Coll, Autophagy as an emerging arena for plant-pathogen interactions. *Curr. Opin. Plant Biol.* **38**, 117–123 (2017).
46. B. Derrien *et al*., A suppressor screen for AGO1 degradation by the viral F-box P0 protein uncovers a role for AGO DUF1785 in sRNA duplex unwinding. *Plant Cell* **30**, 1353–1374 (2018).
47. P. Brodersen *et al*., Isoprenoid biosynthesis is required for miRNA function and affects membrane association of ARGONAUTE 1 in *Arabidopsis*. *Proc. Natl. Acad. Sci. U.S.A.* **109**, 1778–1783 (2012).
48. S. Li *et al*., Biogenesis of phased siRNAs on membrane-bound polysomes in *Arabidopsis*. *Elife* **5**, 1–24 (2016).
49. A. R. Thompson, J. H. Doelling, A. Suttangkakul, R. D. Vierstra, Autophagic nutrient recycling in Arabidopsis directed by the ATG8 and ATG12 conjugation pathways. *Plant Physiol.* **138**, 2097–2110 (2005).

50. P. Bonvini, E. Zorzi, G. Basso, A. Rosolen, Bortezomib-mediated 26S proteasome inhibition causes cell-cycle arrest and induces apoptosis in CD-30+ anaplastic large cell lymphoma. *Leukemia* **21**, 838–842 (2007).
51. T. Potuschak *et al*., EIN3-dependent regulation of plant ethylene hormone signaling by two *Arabidopsis* F box proteins: EBF1 and EBF2. *Cell* **115**, 679–689 (2003).
52. K. Earley, M. Smith, R. Weber, B. Gregory, R. Poethig, An endogenous F-box protein regulates ARGONAUTE1 in *Arabidopsis thaliana*. *Silence* **1**, 15 (2010).
53. T. Regnault, J.-M. Davière, D. Heintz, T. Lange, P. Achard, The gibberellin biosynthetic genes *AtKAO1* and *AtKAO2* have overlapping roles throughout *Arabidopsis* development. *Plant J.* **80**, 462–474 (2014).
54. T. Elmayan *et al*., Arabidopsis mutants impaired in cosuppression. *Plant Cell* **10**, 1747–1758 (1998).
55. I. Gy *et al*., *Arabidopsis* FIERY1, XRN2, and XRN3 are endogenous RNA silencing suppressors. *Plant Cell* **19**, 3451–3461 (2007).
56. A. E. Martínez de Alba, V. Jauvion, A. C. Mallory, N. Bouteiller, H. Vaucheret, The miRNA pathway limits AGO1 availability during siRNA-mediated PTGS defense against exogenous RNA. *Nucleic Acids Res.* **39**, 9339–9344 (2011).
57. Y. J. Kim, A. Maizel, X. Chen, Traffic into silence: Endomembranes and post-transcriptional RNA silencing. *EMBO J.* **33**, 968–980 (2014).
58. A. K. L. Leung, The whereabouts of microRNA actions: Cytoplasm and beyond. *Trends Cell Biol.* **25**, 601–610 (2015).
59. N. G. Bologna *et al*., Nucleo-cytosolic shuttling of ARGONAUTE1 prompts a revised model of the plant MicroRNA pathway. *Mol. Cell* **69**, 709–719.e5 (2018).
60. P. H. Wu, M. Isaji, R. W. Carthew, Functionally diverse microRNA effector complexes are regulated by extracellular signaling. *Mol. Cell* **52**, 113–123 (2013).
61. L. Stalder *et al*., The rough endoplasmatic reticulum is a central nucleation site of siRNA-mediated RNA silencing. *EMBO J.* **32**, 1115–1127 (2013).
62. J. R. Skaar, J. K. Pagan, M. Pagano, Mechanisms and function of substrate recruitment by F-box proteins. *Nat. Rev. Mol. Cell Biol.* **14**, 369–381 (2013).
63. T. M. Nolan *et al*., Selective autophagy of BES1 mediated by DSK2 balances plant growth and survival. *Dev. Cell* **41**, 33–46.e7 (2017).
64. H. Vaucheret, A. C. Mallory, D. P. Bartel, AGO1 homeostasis entails coexpression of MIR168 and AGO1 and preferential stabilization of miR168 by AGO1. *Mol. Cell* **22**, 129–136 (2006).
65. H. Chino, T. Hatta, T. Natsume, N. Mizushima, Intrinsically disordered protein TEX264 mediates ER-phagy. *Mol. Cell* **74**, 909–921.e6 (2019).
66. I. M. Z. Sjøgaard *et al*., The transmembrane autophagy cargo receptors ATI1 and ATI2 interact with ATG8 through intrinsically disordered regions with distinct biophysical properties. *Biochem. J.* **476**, 449–465 (2019).
67. J. Xu, R. Camfield, S. M. Gorski, The interplay between exosomes and autophagy – Partners in crime. *J. Cell Sci.* **131**, jcs215210 (2018).
68. K. Kalinowska, E. Isono, All roads lead to the vacuole-autophagic transport as part of the endomembrane trafficking network in plants. *J. Exp. Bot.* **69**, 1313–1324 (2018).
69. Y. Nishida *et al*., Discovery of Atg5/Atg7-independent alternative macroautophagy. *Nature* **461**, 654–658 (2009).
70. M. Johnston, M.-C. Geoffroy, A. Sobala, R. Hay, G. Hutvagner, HSP90 protein stabilizes unloaded argonaute complexes and microscopic P-bodies in human cells. *Mol. Biol. Cell* **21**, 1462–1469 (2010).
71. D. Gibbings *et al*., Selective autophagy degrades DICER and AGO2 and regulates miRNA activity. *Nat. Cell Biol.* **14**, 1314–1321 (2012).
72. Y. Haxim *et al*., Autophagy functions as an antiviral mechanism against geminiviruses in plants. *eLife* **6**, e23897 (2017).
73. F. Li *et al*., Beclin1 restricts RNA virus infection in plants through suppression and degradation of the viral polymerase. *Nat. Commun.* **9**, 1268 (2018).
74. A. Hafrén *et al*., Turnip mosaic virus counteracts selective autophagy of the viral silencing suppressor HCpro. *Plant Physiol.* **176**, 649–662 (2018).
75. X. Cheng, A. Wang, The potyvirus silencing suppressor protein VPg mediates degradation of SGS3 via ubiquitination and autophagy pathways. *J. Virol.* **91**, e01478-16 (2016).
76. J. Zuo, Q. W. Niu, N. H. Chua, Technical advance: An estrogen receptor-based transactivator XVE mediates highly inducible gene expression in transgenic plants. *Plant J.* **24**, 265–273 (2000).
77. A. Sarrion-Perdigones, J. Palaci, A. Granell, D. Orzaez, Design and construction of multigenic constructs for plant biotechnology using the GoldenBraid cloning strategy. *Methods Mol. Biol.* **1116**, 133–151 (2014).
78. R. A. Johnson, V. Gurevich, S. Filler, A. Samach, A. A. Levy, Comparative assessments of CRISPR-Cas nucleases' cleavage efficiency in planta. *Plant Mol. Biol.* **87**, 143–156 (2015).